Journal of Catalysis 275 (2010) 117–128

Contents lists available at ScienceDirect

Journal of Catalysis

journal homepage: www.elsevier.com/locate/jcat

Temperature-programmed reduction of unpromoted MoS_2-based hydrodesulfurization catalysts: First-principles kinetic Monte Carlo simulations and comparison with experiments

Nicolas Dinter [a], Marko Rusanen [a], Pascal Raybaud [b], Slavik Kasztelan [b], Pedro da Silva [b], Hervé Toulhoat [c,*]

[a] Direction Chimie et Physico-Chimie Appliquées, IFP, 1 & 4 Avenue de Bois-Préau, 92852 Rueil-Malmaison cedex, France
[b] Direction Catalyse et Séparation, IFP, Rond-point de l'échangeur de Solaize BP 3, 69360 Solaize, France
[c] Direction Scientifique, IFP, 1 & 4 Avenue de Bois-Préau, 92852 Rueil-Malmaison cedex, France

ARTICLE INFO

Article history:
Received 9 March 2010
Revised 9 July 2010
Accepted 22 July 2010

Keywords:
Kinetic Monte Carlo simulations
Density functional theory
HDS catalysts activation
Temperature-programmed reduction

ABSTRACT

We present the first kinetic Monte Carlo (kMC) simulations of elementary processes corresponding to temperature-programmed reduction (TPR) experiments of unpromoted MoS_2-based γ-Al_2O_3-supported hydrodesulfurization catalysts. The active Mo-edge surfaces in interaction with the gas phase are represented by a one-dimensional periodic array of alternating "top" and "bridge" sites covered by surface species involved in the pathways connecting dissociative adsorption of dihydrogen and associative desorption of hydrogen sulfide. The simulations are monitored by setting partial pressures of H_2 and H_2S, and temperature or rate of temperature increase. Configuration energies and transition barriers computed by DFT were supplemented by a semi-empirical bond-counting scheme and Brönsted–Evans–Polanyi relationships. Simulated TPR spectra closely match the experimental results.

1. Introduction

The continuous improvement of MoS_2-based catalysts requires a deeper understanding of the chemical reactivity of active sites located at the MoS_2 nanocrystallite edges. Temperature-programmed reduction (TPR) is one of the experimental techniques most often used in the field (cited by several hundreds of papers), enabling experimentalists working in hydrodesulfurization catalysis to gain insights into the stability of sulfided species present on the transition metal sulfides in the presence of a reductive environment, mimicking the reaction conditions. The removal of these sulfided species, released in the form of H_2S, is accompanied by reasonably well-defined hydrogen consumption peaks: the lower-temperature peaks ("weakly bonded sulfur") may be viewed as the signature of the activation of potential sites present at the surface of the catalysis, whereas higher-temperature peaks may be attributed to the reduction of the bulk materials. Recently, Afanasiev [1] proposed an interpretation of the higher-temperature peak attributed to the bulk reduction peak on the basis of the evaluation of the enthalpy of reduction. In contrast, the lower-temperature peaks corresponding to S-species located at the surface are often rather ambiguously attributed to so-called "weakly bonded S-species", which eludes the questions regarding either the precise nature of the S-species (physisorbed vs chemisorbed H_2S, chemisorbed SH^- or S^{2-} species) or their localization at the edges of the MoS_2 crystallites. TPR experimental data (particularly the temperature position of hydrogen consumption peaks, hydrogen consumption) remain thus subject to open questions. Moreover, the challenge remains to furnish an unambiguous description of the elementary chemical events taking place at the edges of the MoS_2 nanocrystallites during the reduction process. In particular, determining the precise nature and location of the sulfur species removed from the catalytic materials is a key question for the further identification of the potential active sites.

In the related previous paper [2], we have reported experiments and kinetic modeling of the temperature-programmed reduction of a series of gamma-alumina-supported unpromoted MoS_2-based hydrodesulfurization (HDS) catalysts with Mo loadings in the range 4–22 wt.%. These catalysts were pre-sulfided in conditions of high chemical potential of sulfur, in which the 100% S-covered Mo-edge prevails, leading to triangular-supported nanoparticles of the active-phase MoS_2 [3–7]. TPR experiments under a flowing mixture of 10% H_2 + 90% Ar have revealed H_2 consumption (H_2S production) profiles with a narrow first peak (P1) at a lower temperature TP1 (521–552 K) and a broad composite second peak (P2) at a higher temperature TP2 (750–940 K). TP1 decreases as Mo loading increases. We have assigned

* Corresponding author. Fax: +33 0 1 47 52 70 22.
E-mail address: herve.toulhoat@ifp.fr (H. Toulhoat).

0021-9517/$ - see front matter © 2010 Elsevier Inc. All rights reserved.
doi:10.1016/j.jcat.2010.07.020

this first peak to the reductive elimination of one edge S per Mo in the form of H_2S, the S-edge coverage decreasing from 100% to 50%. We have performed a detailed DFT study of this reaction pathway, allowing accurate first-principles determination of intermediates and transition states, and the associated energy barriers. We have identified the rate-limiting step (*rls*) as the dissociative homolytic adsorption of H_2 on one S_2 top dimer resulting in the formation of two adjacent top SSH groups. We have developed a kinetic analysis of the TPR experiments, making use of the DFT data as input, which allows a precise matching of P1 profiles for all investigated catalysts: the slight variation of TP1 and of P1 shapes is very well explained by the combined effects of MoS_2 nanoparticle sizes and number by unit surface area (area densities), both determined by Mo loading.

As already shown by several authors [8–13], first-principles kMC simulations offer an efficient strategy to bridge the gap between the picture furnished by static density functional theory (DFT) at the microscopic scale and the dynamic behavior of the working catalyst surface under given operating conditions (temperature, partial pressures of reactants and products in fluid phase). Reliable statistical estimates of macroscopic rates of reaction can thus be compared with experimental observables.

In this report, we present kinetic Monte Carlo (kMC) simulations of the TPR experiments described in [2], the latter providing a good basis for assessing the validity of the assumptions involved in these simulations. To the best of our knowledge, kMC simulations of catalytic processes at MoS_2 edge sites are addressed here for the first time. Consequently, a rather detailed methodology section explains the formalism and hypotheses of the kMC simulation. Indeed, our main purpose here is to demonstrate the feasibility of first-principles-based kMC for bringing additional understanding of the working hydrotreating catalyst. Future works will have on the one hand to extend the present approach to unpromoted S-edges, and M-edges and S-edges promoted by Co or Ni, and on the other hand go beyond the mere dissociative activation of H_2 into various hydrogenated surface species, in order to include the reactions of the latter with adsorbed hetero-aromatic compounds.

Our report is thus organized as follows:

The methods section comprises the following subsections:

- Description of the kMC algorithm used and its implementation, including a discussion on the procedure adopted to sample optimally the simulated H_2 consumptions in the course of a simulated TPR.
- Description of the model chosen to represent Mo-edge sites, in DFT and kMC.
- Description of the elementary event rate expressions, as introduced and justified in [2]. Following our previous conclusions, model H3 has been selected to describe dissociative adsorption and associative desorption. The corresponding empirical optimal linear temperature dependence of the fraction of translational-rotational entropy transferred from the gas phase to the physisorbed state is also taken from this model.
- Inventory of all the elementary events considered together with the associated barriers obtained from DFT calculations or interpolated through a simple bond-counting scheme.

In the results section, we present and discuss the kMC simulation results and compare them both to experimental data and to the results of the analytical model given in [2]. Finally, we draw conclusions and describe perspectives for the future applications of first-principles kMC simulations to the improvement of our fundamental knowledge of industrial HDS catalyst activation and of transitory as well as steady-state dynamic behavior at the microscopic scale.

2. Methods

2.1. Kinetic Monte Carlo algorithm

kMC simulations belonging to the class of stochastic simulations require two types of input. A set of elementary events, i.e. dissociative adsorptions, surface diffusions, surface chemical reactions, associative desorptions, occurring on an array of "sites" must be described. All related microscopic intrinsic frequencies (microscopic rates or occurrence probability per unit time, in Hertz) mostly dependent on imposed temperature and chemical potentials must be provided. In the following, the gas phase is assumed to behave as an ideal gas composed of different species i with masses m_i and thus fully described when partial pressures P_i and temperature T are given.

In a simulation, starting from an initial arbitrary configuration, sequences of configurations along the time line are obtained by executing randomly selected elementary events with the appropriate statistical weights, under the constraint that microscopic reversibility is respected. kMC thus describes dynamical processes by a sequence of elementary events, each of them making the system evolve from a state i to a state j. One takes into account only the elementary events listed above, which are relatively rare compared to other local fluctuations at the atomic scale. When such a rare event occurs, it is completely uncorrelated with the previous event. As a consequence, the system follows a Markov chain of states. In other terms, kMC simulations describe the system's temporal evolution by solving the Markovian master equation:

$$\frac{d\Omega_j(t)}{dt} = \sum_i W_{i\leftrightarrow j}\Omega_i(t) - \sum_i W_{j\leftrightarrow i}\Omega_j(t) \tag{1}$$

With $\Omega_i(t)$ the probability to find the system at time t in the state i, $\Omega_j(t)$ the probability to find the system at time t in the state j, $W_{i\leftrightarrow j}$ the probability for the system to evolve to a state j from a state i and $W_{j\leftrightarrow i}$ the probability for the system to evolve to a state i from a state i.

To fulfill the detailed balance condition (microscopic reversibility), each process has to be counterbalanced by its reverse process. The rate of a given process characterizes the probability per unit time for the system to evolve through this particular process. The simulated system is allowed to evolve according to the Bortz, Kalos and Lebowitz (BKL) algorithm [14], described in Fig. 1:

i. from a given configuration, all possible processes are listed and the associated rates are determined,
ii. the sum R of all possible process rates k_i is calculated,
iii. a process is picked at random and executed,
iv. the clock time t is updated by a stochastic time step δt [15],
v. the procedure is repeated until the desired maximum simulated time t_{max} is reached.

Let $\rho_1 \in]0, 1[$ be a first random number, and p the label of process of rate k_p belonging to the list established at step i. Step iii is executed after p has been determined in an internal loop according to inequalities in the following equation:

$$\sum_{i=0}^{p-1} k_i < \rho_1 R \leqslant \sum_{i=0}^{p} k_i \tag{2}$$

In this way, the probability for choosing the process "p" is weighted by its normalized rate k_p/R. In other words, a process with a large rate has a greater chance to be chosen than a process with a smaller rate. Notice that the list of possible processes and the associated total rate change for every cycle.

Step iv is executed according to Eq. (3), where $\rho_2 \in]0, 1[$ is a second independent random number. This equation accounts for

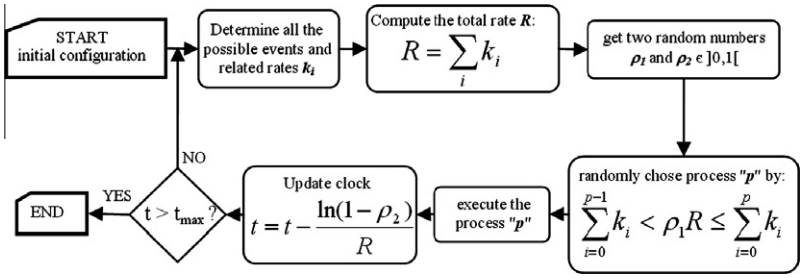

Fig. 1. Bortz, Kalos and Lebowitz algorithm flow chart.

the fact that the time of survival of any particular configuration is a random variable following a Poisson distribution (according to BKL [14]).

$$\delta t = -\frac{\ln(1-\rho_2)}{R} \tag{3}$$

Once the time increment has been completed and one returns to step i, the list of events and associated rates must be updated. Consequently, the whole array of sites must be scanned and for each site, all authorized events must be identified. Any given event is associated with a particular site. Therefore, each rate corresponds to only one site, while a given site may be associated with several rates. Both the partial sums $\sum k_i$ and the total sum R are computed and stored along with the results of scanning the surface, so that step iii becomes straightforward. In practice, the most complex and demanding in computer resources is step i.

The random numbers ρ_1 and ρ_2 are uniformly chosen within]0, 1[with a Mersene Twister random number generator developed by Matsumoto et al. [16]. This generator has a very large period $2^{19937} - 1 \approx 10^{6000}$ which ensures that there is no correlation between the random numbers.

2.2. Statistical treatment of TPR simulation results

Statistics are obtained by averaging data points collected during a set of runs using a post-treatment script. For TPR simulations, each data point reported is an average within a pre-defined temperature range δT over p independent simulations performed in a specified temperature range ΔT.

In a simulation of rank i, $1 \leq i \leq p$, over ΔT, the total number of steps N_i is a random variable, as are the corresponding N_i temperature increments and elementary reactant (e.g. hydrogen) consumptions y_i. One is thus facing the problem of optimizing the width δT of the temperature "bins", or, in other terms, of setting the number L of such bins per simulation, with $\Delta T = L \cdot \delta T$.

Let us first assume that the width of elementary temperature increments (or time steps) is uniformly distributed over ΔT. Let $\langle N \rangle$ be the average of N_i. The value of δT sets the resolution of the analysis on the abscissa, since it can be considered as the maximum absolute error on temperature. Therefore, the resolution δT scales as L^{-1}. Each bin will contain, on average, $q = p\langle N \rangle / L$ values of y. One will aim at minimizing, for each bin, the standard deviation of the average of the computed values of y, denoted as $\sigma(\langle y \rangle)$. The latter scales as $q^{-1/2}$, therefore as $(p\langle N \rangle)^{-1/2} L^{1/2}$. Since the scaling laws for $\sigma(\langle y \rangle)$ and δT are strictly increasing and decreasing respectively for L positive, the best compromise in L will be found at their intersection, so that the optimal value L^* is given by the following equation:

$$L^* = (p\langle N \rangle)^{1/3} \tag{4}$$

Hence, $q^* = (p\langle N \rangle)^{2/3}$. It results that $\sigma(\langle y \rangle)$ scales as $(p\langle N \rangle)^{-1/3}$ or $1/L^*$. Moreover, over an interval δT, the standard deviations $\sigma(y)$ of the values of y and $\sigma(T)$ of the values of T are correlated by the relation $\sigma(y) = m(T_k)\sigma(T)$, where $m(T_k)$ is the local slope of the underlying relationship $y(T)$, and T_k is the temperature at the center of the current interval δT. Since δT is an upper bound of $\sigma(T)$, one has:

$$\sigma(y_k) \leqslant \frac{m(T_k)\Delta T}{(p\langle N \rangle)^{1/3}} \tag{5}$$

Eq. (5) gives a criterion to choose p, so as to provide an upper bound to the maximal fluctuation for a simulated data point. In the following, typical values will be $\Delta T = 225$ K, $\langle N \rangle = 10^6$ and $m(T_k)$ at the inflexion point of the TPR peaks of the order of 10^{-5} mol g^{-1} s^{-1} K^{-1}. Therefore, with $p = 5$, an upper bound for $\sigma(y)$ is $\sim 2 \times 10^{-5}$ mol g^{-1} s^{-1}, whereas $\langle y \rangle$ at the inflexion point is $\sim 5 \times 10^{-5}$ mol g^{-1} s^{-1}, so that the maximum amplitude of the relative fluctuation around the average value, approximated by $2\sigma(y)/\langle y \rangle$, is ~100%. With $p = 10$, it improves to ~79%. For a given bin among the total of $L^* = 215$, the average value of y is moreover computed over $p\langle N \rangle / L^* \sim 46{,}000$ estimates and is therefore quite precise. According to the previous result on the scaling of $\sigma(y)$ as $1/L^*$, an upper bound estimate of the relative error on $\langle y \rangle$ can finally be taken as $2\sigma(y)/(L^*\langle y \rangle)$, hence ~0.6% for $p = 5$ and ~0.37% for $p = 10$.

Additionally, in view of the underlying correlation of y and T in the interval, a systematic error in excess by $m(T_k)[\langle T \rangle_k - T_k]$ is introduced on assigning the center T_k of the corresponding interval of width δT as abscissa to the ordinate $\langle y \rangle_k$. Here, $\langle T \rangle_k$ is the average of temperatures in the bin of rank k. Starting from the series of L^* first estimates for $\langle y \rangle_k$, $1 \leq k \leq L^*$, a series $\langle y^{corr} \rangle_k$ corrected to first order may be generated thanks to the approximation given in the following equation:

$$\langle y^{corr} \rangle_k = \langle y \rangle_k - \left[(\langle y \rangle_{k+1} - \langle y \rangle_{k-1}) \frac{(\langle T \rangle_k - T_k)}{\delta T} \right] \tag{6}$$

2.3. Atomistic models for kMC and DFT

As mentioned in Section 2.1, in kMC, the "real" three-dimensional atomistic model of the catalyst under scrutiny must be mapped onto a specific array of sites or lattice. For MoS_2 nanoparticles, active sites are exclusively located on the edges; therefore, when transposing the slab supercell model used in [2] for DFT calculations, only the outermost Mo layer has to be considered. In addition, MoS_2 single sheets have a thickness of about 3.1 Å, which is low compared to a typical edge length (>31 Å). For this reason, we neglect the corresponding dimension. In order to take into account species which extend across an edge, such as sulfur pairs, we represent them as a particular species on site (e.g. S_2). We adopt one-dimensional periodic lattices representing the edge, involving alternating "top sites", referring to the Mo atom positions, and "bridge sites". A final approximation is that the sites are well defined, or in other words, atoms remain in their positions, and surface reconstructions and relaxations, which are expected to be

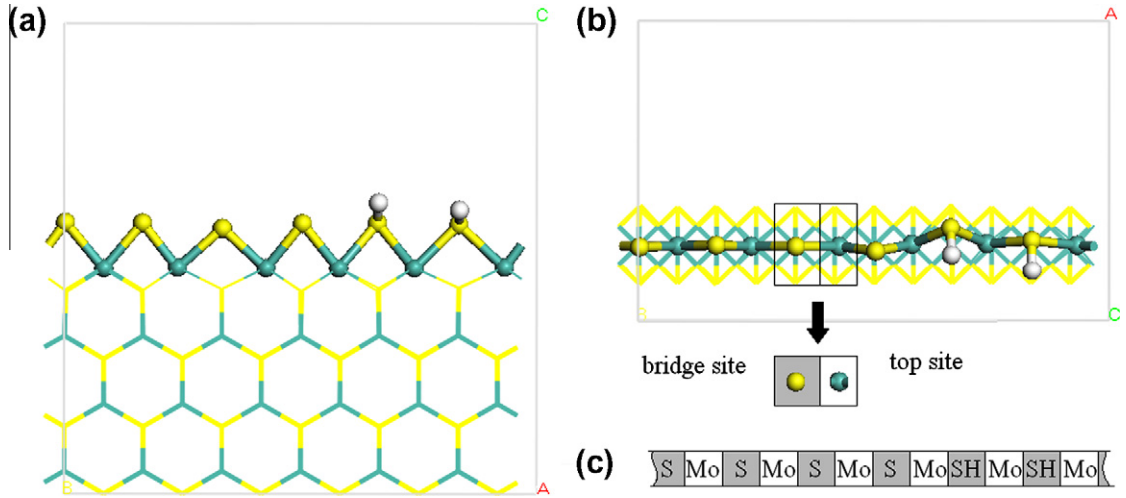

Fig. 2. One-dimensional lattice model construction for a given configuration of the Mo-edge surface. Panel (a) represents a view of the Mo-edge normal to the (*xy*) plane. Atoms and bonds of the active Mo-edge are represented as balls and sticks, others as lines. Legend: (color on line) black spheres (turquoise): molybdenum atoms, gray spheres (yellow): sulfur atoms, white spheres: hydrogen atoms. Panel (b) (same legend) represents a Mo-edge view normal to the (*xz*) plane. Top and bridge sites are highlighted with the rectangular inset. The bridge site is differentiated with a gray background. Panel (c) represents the one-dimensional lattice model for such a configuration. Species are located on the different sites. (For interpretation of the references to color in this figure legend, the reader is referred to the web version of this article.)

minor, are not taken into account in this simplified geometric representation. However, their energetic consequences are reflected in the configuration energies assigned to species at these lattice sites. Fig. 2 summarizes the procedure leading to a 1D-lattice representing a given Mo-edge configuration. All the kMC results presented in this report are obtained using a 1D periodic array of 1000 sites.

The surface species to be considered under a H_2/H_2S atmosphere are the following: M (vacant top sites), S, H, H_2, SH, SH_2, S_2, S_2H and S_2H_2 (sitting on top and bridge sites). The set of elementary processes involving these species on the underlying 1D-lattice is a key ingredient of our kMC model. Here, we consider only the dissociative adsorption of H_2 or H_2S from gas phase, the surface diffusion of surface species and their allowed associative desorption to from H_2 or H_2S. All processes are listed in Table 1, along with the associated forward and reverse energy barriers taken into account, as discussed in the next section. In order to facilitate understanding of our notation of these processes, some of them are schematized in Fig. 3.

2.4. Determination of activation barriers

2.4.1. DFT database

For the processes involved in the reduction by H_2 of S_2 surface dimers on a fully sulfur-covered (100%S) Mo-edge-producing bridging S adatoms and H_2S, we have used the results of our previous DFT calculations, as reported in [2]. To solve the Kohn–Sham equations [17], the Vienna *Ab Initio* simulation package (VASP) [18,19] was used, and further technical details can be found in [2].

Since it cannot be excluded that processes involved in the reduction by H_2 of bridging S adatoms, producing H_2S, occur locally (local S coverage $\leqslant$50%), we have moreover used the results published by Paul et al. [20] and Travert et al. [21], which were also obtained with VASP for very similar atomistic models to those used in [2].

2.4.2. Interpolations of energies via a bond-counting scheme (BCS)

Calculating the barriers for all possible processes and configurations is a formidable task with currently available computing

Table 1
Processes taken into account for kMC simulations with their associated activation barrier. The barrier values given are calculated by DFT [2,20,21], or guessed according to the bond-counting scheme (BCS) in combination or not with BEP relationships as shown in Fig. 7, or deduced by the consistency requirement (CR). Processes 7 and 9 were assumed equivalent. A vacant bridge or top site is denoted by V. Subscripts t and b refer to top and bridge positions respectively (see Fig. 3).

#	Process	$E^{\neq}$ (eV)	Ref.	#	Reverse process	$E^{\neq}$ (eV)	Ref.
Surface diffusion				*Surface diffusion*			
1	$H_t + V_b \rightarrow H_b + V_t$	0.05	BCS	2	$H_b + V_t \rightarrow H_t + V_b$	0.61	CR
Surface associations				*Surface dissociations*			
3	$H_t + S_b \rightarrow V_t + SH_b$	0.25	[21] (12d–f)	4	$V_t + SH_b \rightarrow S_b + H_t$	0.39	[21]
5	$H_b + V_t + S_b \rightarrow V_b + V_t + SH_b$	0.93	[21] (12g–i)	6	$V_b + V_t + SH_b \rightarrow S_b + V_t + H_b$	0.51	CR
7	$H_t + S_{2b} \rightarrow V_t + SHS_b$	0.54	Idem #9	8	$V_t + SHS_b \rightarrow S_{2b} + H_t$	0.50	CR
9	$H_t + SHS_b \rightarrow V_t + SHSH_b$	0.54	[21] (12a–c)	10	$V_t + SHSH_b \rightarrow SHS_b + H_t$	0.50	CR
Dissociative adsorption of H_2				*Associative desorption of H_2*			
11	$H_2 + V_t + V_b + V_t \rightarrow H_t + V_b + H_t$	1.15	BCS + BEP	12	$H_t + V_b + H_t \rightarrow H_2 + V_t + V_b + V_t$	0.51	CR
13	$H_2 + V_b + V_t + V_b \rightarrow H_b + Vt + H_b$	0.00	BCS + BEP	14	$H_b + V_t + H_b \rightarrow H_2 + V_b + V_t + V_b$	0.47	CR
15	$H_2 + V_t + V_b \rightarrow H_t + H_b$	0.55	BCS + BEP	16	$H_t + H_b \rightarrow H_2 + V_t + V_b$	0.46	CR
17	$H_2 + S_b + V_t \rightarrow H_t + SH_b$	0.97	[20]	18	$H_t + SH_b \rightarrow H_2 + S_b + V_t$	0.60	[20]
19	$H_2 + S_b + V_t + V_b \rightarrow SH_b + V_t + H_b$	0.55	[20]	20	$SH_b + V_t + H_b \rightarrow H_2 + S_b + V_t + V_b$	0.60	[20]
21	$S_{2t} + H_2 \rightarrow SHSH_t$	0.95	[2]	22	$SHSH_t \rightarrow H_2 + S_{2t}$	0.83	[2]
Dissociative adsorption of H_2S				*Associative desorption of H_2S*			
23	$H_2S + V_t + V_b + V_t \rightarrow SH_b + V_t + H_b$	0.09	[20]	24	$SH_b + V_t + H_b \rightarrow H_2S + V_t + V_b + V_t$	2.41	[20]
25	$H_2S + V_b + V_t \rightarrow SH_b + H_t$	0.09	[20]	26	$SH_b + H_t \rightarrow H_2S + V_b + V_t$	1.00	[20]
27	$S_{2b} + S_t + S_{2b} + H_2S \rightarrow S_{2b} + SHSH_t + S_{2b}$	0.46	[2]	28	$S_{2b} + SHSH_t + S_{2b} \rightarrow H_2S + S_{2b} + S_t + S_{2b}$	0.73	[21]

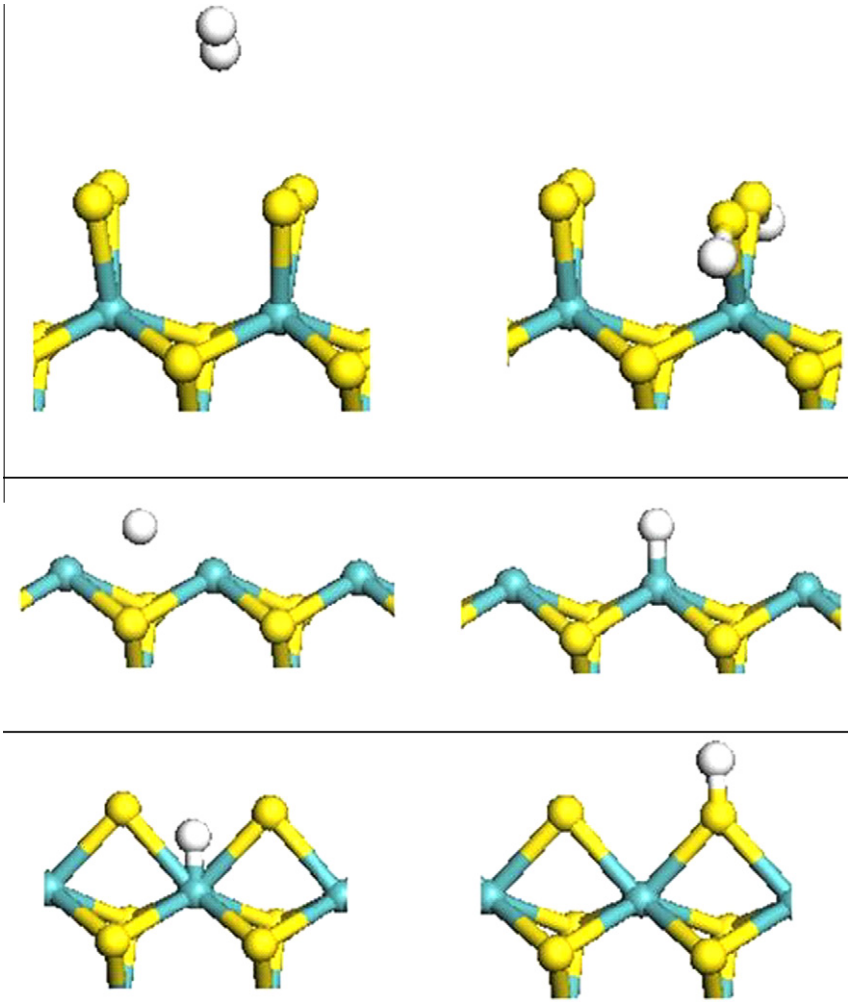

Fig. 3. Examples of elementary processes taken into account in the kMC simulations. From top to bottom: $S_{2t} + H_2 \rightarrow SHSH_t$, $H_b + V_t \rightarrow H_t + V_b$, $H_t + S_b \rightarrow V_t + SH_b$.

resources. Approximations can however be developed reproducing the available DFT results and enabling the prediction of energies for configurations comparable to those explicitly studied from first-principles. We have used here a simple "bond-counting scheme" (BCS), wherein we assume that bond energies are conserved during surface processes. We have applied this scheme for processes and configurations involving local S coverages $\leqslant$50%, namely the reduction of bridging S adatoms. Examples of such

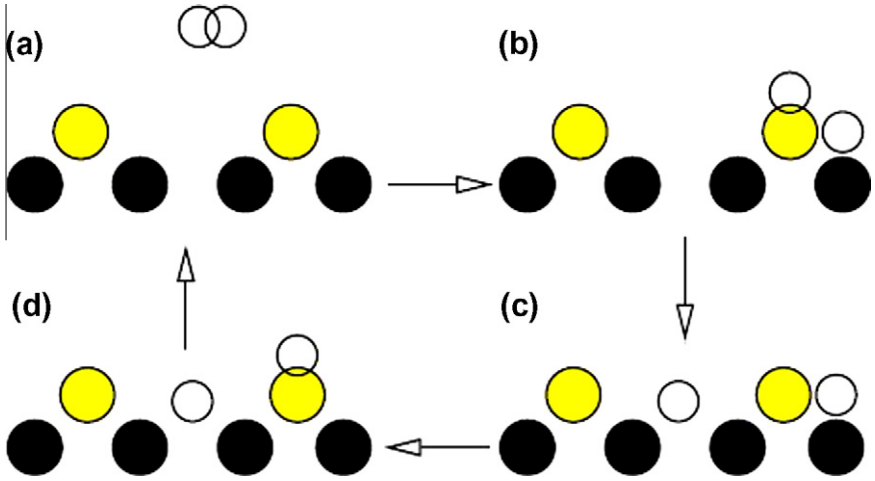

Fig. 4. Schematic representation of the Krebs cycle for $\Delta E_0 = E_c - E_b$. From (a) to (b) H_2 dissociatively adsorbs onto a bridging S with a vacancy as nearest neighbor; from (b) to (c) one SH-group dissociates such that the H fills the vacancy, and there is a H atom as a neighbor of SH-group before SH dissociation takes place; from (c) to (d) a SH-group is created; finally from (d) to (a) H_2 desorbs associatively from the surface leaving a vacancy. The DFT values [20,21] for the changes in the total energy are $\Delta E_{ba} = 0.37$ eV, $\Delta E_{dc} = -0.14$ eV, and $\Delta E_{ad} = 0.05$ eV.

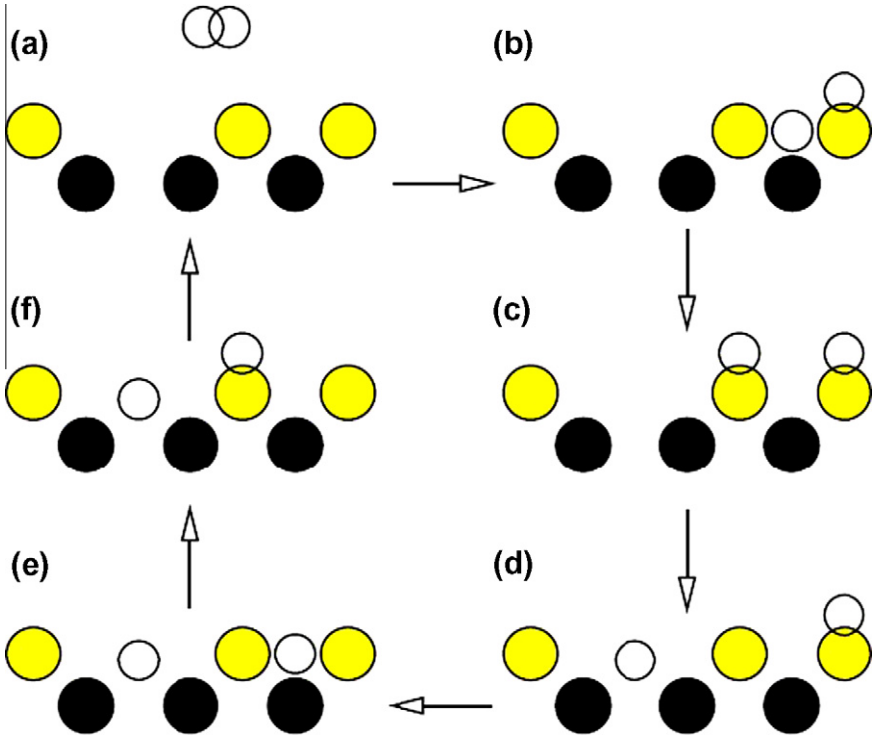

Fig. 5. Schematic representation of the Krebs cycle for $\Delta E_1 = E_d - E_c$. Note the difference from Fig. 4: in the present case there is no H atom as a neighbor of a SH-group before dissociation. The DFT values [20,21] are $\Delta E_{ba} = 0.37$ eV, $\Delta E_{cb} = 0.0$ eV, $\Delta E_{ed} = 0.14$ eV, $\Delta E_{fe} = -0.14$ eV, and $\Delta E_{af} = 0.05$ eV.

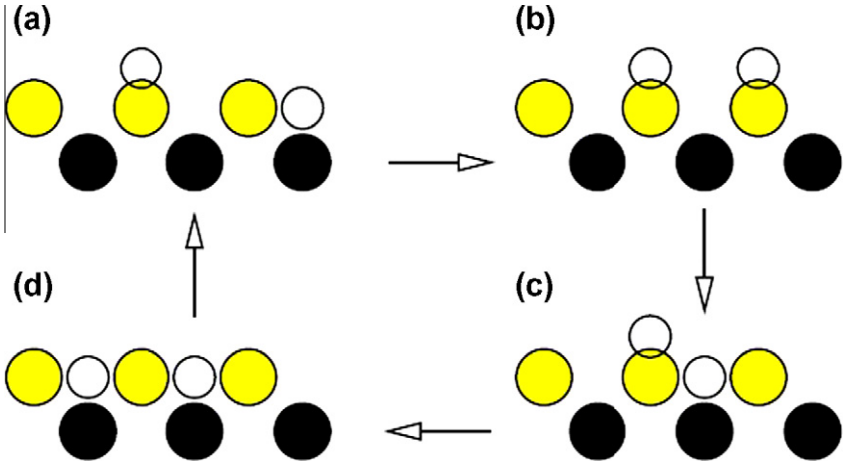

Fig. 6. Schematic representation of the Krebs cycle for $\Delta E_2 = E_d - E_c$. The DFT values [20,21] are $\Delta E_{ba} = -0.14$ eV, $\Delta E_{cb} = 0.0$ eV, and $\Delta E_{ad} = -0.14$ eV.

processes are illustrated in Figs. 4–6, which represent selected Krebs cycles.

Let us associate bond strengths a with each S–H group, b with each Mo–H group and c with each neighboring Mo–H/S–H groups, such that a bond exists, if the corresponding group exists within the local neighborhood. The word "bond" must be understood here as denoting existence of an interaction energy, which could be interpreted as a chemical bond (for instance, a "bond" of very low energy between a Mo–H group and an S–H group). For convenience, all energy values are measured in units of $E_{bond} = 0.14$ eV as justified below. This means that, for example, an energy difference -0.28 eV converts into -2.

Consider the reactions (b) → (c), (c) → (d) and (c) → (d) which close the Krebs cycles represented in Figs. 4–6 respectively. Using the reaction energies calculated by DFT for the other steps in these cycles, energy conservation allows to deduce:

$$\Delta E_0 = E_c - E_b = -0.28 \text{ eV}$$
$$\Delta E_1 = E_d - E_c = -0.42 \text{ eV}$$
$$\Delta E_2 = E_d - E_c = 0.28 \text{ eV}$$

Counting the changes in the bond numbers between the initial and final states in the reaction energies ΔE_0, ΔE_1 and ΔE_2, and adopting the energy unit E_{bond}, the previous reaction energies can also be expressed as bond energy balances, leading to the following system of three linear equations with three unknown variables:

$$-a + 2b - c = -2 \quad (7)$$
$$-a + 2b = -3 \quad (8)$$
$$-a + b - c = 2 \quad (9)$$

the solution of which is $a = -5$, $b = -4$, $c = -1$. This solution of our bond-counting scheme thus implies that after every transition taking place on a surface, the total energy changes as:

$$\Delta E_{fi} = -\left[5\Delta n_{fi}^{S-H} + 4\Delta n_{fi}^{Mo-H} + \Delta n_{fi}^{S-H/Mo-H}\right] E_{bond} \quad (10)$$

where $\Delta E_{fi} \equiv (E_{final} - E_{initial})$, and the quantity $\Delta n_{fi}^{Mo-H} \equiv (n_f^{Mo-H} - n_i^{Mo-H})$ is the difference between the number of Mo–H groups in the local neighborhood of a site in the final and initial states (including the site itself), with similar expressions for S–H groups and the nearest-neighbor S–H/Mo–H groups. It must be emphasized that it is assumed that the local energy changes are due only to differences in the nearest neighbors. This seems to be a reasonable choice since in the DFT calculations, the cell size is also rather limited.

2.4.3. Interpolations with Brönsted–Evans–Polanyi (BEP) relationships

BEP relationships are linear relationships, Eq. (11), observed between activation barriers $E^{\neq} = E_T - E_A$ and energy changes $\Delta E = E_B - E_A$ in a process $A \rightarrow T \rightarrow B$, where A is a reactant, B a product and T the transition state.

$$E^{\neq} = \mu \Delta E + \lambda \quad (11)$$

Such relationships have been theoretically postulated for certain cases [22–24]. More recently, many convincing examples have emerged from DFT studies on model systems [25–29]. When occurring for a homologous class of processes, BEP linear correlations may be used to estimate barriers from energy differences between initial and final states. In the present work, we have in some cases combined the BCS scheme, providing estimates of energy changes, with BEP relationships.

2.5. Rate expressions for elementary events

We have conserved the same notation as in [2]. All rates are described within the formalism of the transition-state theory (TST).

For surface diffusion, association and dissociation processes (processes #1–10 in Table 1), the rates are described by the following equation:

$$k_i = \frac{k_B T}{h} \frac{q_{vib}^{TS}}{q_{vib}^{init}} \exp\left(\frac{-E^{\neq}}{k_B T}\right) \quad (12)$$

with k_B and h the Boltzmann and Planck constants, respectively, T the absolute temperature, q_{vib}^{TS} and q_{vib}^{init} the vibrational partition functions for, respectively, the TS and initial sate, and $E^{\neq}$ the barrier.

In order to represent dissociative adsorptions of H_2 and H_2S and their reverse processes, associative desorptions, (processes 11–28 in Table 1), we have reconsidered and refined the model H3 proposed in our previous paper [2]. In what follows, we develop in the same spirit the appropriate expressions for the rates of these "pseudo-elementary" events and we demonstrate that these rates satisfy the micro-reversibility principle.

We introduce the coverages $\theta_{\phi,H_2}, \theta_{\phi,H_2S}, \theta_\chi$ by physisorbed and chemisorbed (dissociated) reactant, respectively (e.g. H_2, H_2S), θ_S^* and θ_V^* the fraction of empty sites on the initial M-edge 100%S and final M-edge 50%S surfaces, respectively. The coverages by chemisorbed configurations distinct from the most stable one (two H-bonded neighbor S–Mo–SH according to our DFT calculations as reported in Fig. 4 of [2]) are neglected. In this model, the balance of coverages yields:

$$\theta_S^* + \theta_{\phi,H_2} + \theta_\chi + \theta_{\phi,H_2S} + \theta_V^* = 1 \quad (13)$$

Assuming the system is very close to equilibrium, one has:

$$\frac{\theta_{\phi,H_2}}{\theta_S^*} = K_{H_2,g\rightarrow\phi}^{eq} = \exp\left(\frac{-\Delta G_{H_2,g\rightarrow\phi}}{k_B T}\right) \quad (14)$$

$$\frac{\theta_\chi}{\theta_S^*} = K_{H_2,g\rightarrow\chi}^{eq} = \exp\left(\frac{-\Delta G_{H_2,g\rightarrow\chi}}{k_B T}\right) \quad (15)$$

$$\frac{\theta_{\phi,H_2S}}{\theta_V^*} = K_{H_2S,g\rightarrow\phi}^{eq} = \exp\left(\frac{-\Delta G_{H_2S,g\rightarrow\phi}}{k_B T}\right) \quad (16)$$

$$\frac{\theta_\chi}{\theta_V^*} = K_{H_2S,g\rightarrow\chi}^{eq} = \exp\left(\frac{-\Delta G_{H_2S,g\rightarrow\chi}}{k_B T}\right) \quad (17)$$

where $K_{H_2,g\rightarrow\phi}^{eq}, K_{H_2S,g\rightarrow\phi}^{eq}$ are the equilibrium constants for physisorption, $\Delta G_{H_2,g\rightarrow\phi}, \Delta G_{H_2S,g\rightarrow\phi}$ the free-energy variations associated with the physisorption processes, $K_{H_2,g\rightarrow\chi}^{eq}, K_{H_2S,g\rightarrow\chi}^{eq}$ the equilibrium constants for chemisorption and $\Delta G_{H_2,g\rightarrow\chi}, \Delta G_{H_2,g\rightarrow\chi}$, the free-energy variations associated to the chemisorption processes, relative to H_2 and H_2S, respectively. We have therefore assumed that H_2S physisorbs on M-edge 50%S (sites indiced V), and H_2 on M-edge 100%S (sites indiced S), without competition. The system of equations (13)–(17) is determined and allows to express the coverages by free sites:

$$\theta_V^* = \theta_S^* \exp\left(\frac{-(\Delta\mu_{H_2}^g - \Delta\mu_{H_2S}^g)}{k_B T}\right) \quad (18)$$

$$\theta_S^* = \frac{1}{\left[1 + \exp\left(\frac{-\Delta G_{H_2,g\rightarrow\phi}}{k_B T}\right) + \exp\left(\frac{-\Delta G_{H_2,g\rightarrow\chi}}{k_B T}\right) + \left[1 + \exp\left(\frac{-\Delta G_{H_2S,g\rightarrow\phi}}{k_B T}\right)\right] \exp\left(\frac{-(\Delta\mu_{H_2}^g - \Delta\mu_{H_2S}^g)}{k_B T}\right)\right]} \quad (19)$$

where $\Delta\mu_{H_2}^g$ and $\Delta\mu_{H_2S}^g$ are the chemical potentials of H_2 and H_2S in gas phase, respectively, as given by Eq. (SM3).

Further, within the steady-state approximation and keeping the notations adopted in [2], the equation for the rate of dissociative adsorption of H_2 on the empty sites of M-edge 100%S, k_{da,H_2} is:

$$k_{da,H_2} = \left(\frac{A_{st}}{A_{uc}}\right) \frac{k_{H_2,g\rightarrow\phi}^{KTG} k_{H_2,\phi\rightarrow\chi}}{k_{H_2,g\rightarrow\phi}^{KTG}\left(\frac{\theta_S^*}{\theta_{H_2,\phi}}\right) + k_{H_2,\phi\rightarrow\chi}} \theta_S^* \quad (20)$$

where the prefactor $\frac{A_{st}}{A_{uc}}$ is the ratio of the area available for reactive adsorption to the total area available for adsorption, as explicited by Eq. (11) of [2] and also provided as Eqs. (SM1) and (SM2) in Supplementary materials. $k_{H_2,g\rightarrow\phi}^{KTG}$ is the physisorption rate constant for H_2, as provided by the kinetic theory of gases and $k_{H_2,\phi\rightarrow\chi}$ is the microscopic rate constant for chemisorption of H_2 (e.g. homolytic dissociation of dihydrogen). A similar equation can be written for the dissociative adsorption of H_2S on empty sites of the M-edge 50%S, with the proper indices and replacing θ_S^* by θ_V^*.

Now, following Eq. (5) of [2] and making implicit the indices referring to H_2 or H_2S:

$$k_{\phi\rightarrow\chi} = \frac{k_B T}{h} \exp\left(\frac{-\Delta G_{\phi\rightarrow\chi}^{\neq}}{k_B T}\right) \quad (21)$$

$$k_{\chi\rightarrow\phi} = \frac{k_B T}{h} \exp\left(\frac{-\Delta G_{\chi\rightarrow\phi}^{\neq}}{k_B T}\right) \quad (22)$$

where $\Delta G_{\phi\rightarrow\chi}^{\neq}$ is the free-energy barrier to dissociation, starting from the physisorbed state, and $\Delta G_{\chi\rightarrow\phi}^{\neq}$ is the reverse free-energy barrier to association, starting from the dissociated chemisorbed state. With $f[T, \theta_S]$, the fraction of the translational–rotational free-energy transferred from the gas phase to the (mobile) physisorbed state, as introduced in [2], one may write:

$$\Delta G_{\phi\rightarrow\chi}^{\neq} = E_{\phi\rightarrow\chi}^{\neq} + G_{\phi\rightarrow\chi}^{TS} - f[T,\theta_S]\Delta\mu \quad (23)$$

$$\Delta G_{g\rightarrow\phi} = E_{b,\phi} - (1 - f[T,\theta_S])\Delta\mu \quad (24)$$

$$\Delta G_{\chi\rightarrow\phi}^{\neq} = E_{\chi\rightarrow\phi}^{\neq} + G_{\phi\rightarrow\chi}^{TS} - G_\chi \quad (25)$$

$$\Delta G_{g\rightarrow\chi} = E_{b,\chi} + G_\chi - \Delta\mu \quad (26)$$

where $E^{\neq}_{\phi\to\chi}$ is the electronic energy barrier to dissociation, $G^{TS}_{\phi\to\chi}$ the vibrational correction to the free-energy at the transition state for dissociation, G_χ the vibrational correction to the free-energy at the dissociated chemisorbed state, $E_{b,\phi}$ the binding energy of the physisorbed state, $E_{b,\chi}$ the binding energy of the dissociated chemisorbed state and $\Delta\mu$ the translational-rotational free-energy in gas phase. (Eq. (SM3)).

Our DFT evaluations of $E_{b,\phi}$ for H_2 at M-edge 100%S and H_2S at M-edge 50%S gave −0.2 eV and −0.12 eV, respectively, and of $E_{b,\chi}$ for H_2 at M-edge 100%S and H_2S at M-edge 50%S −0.08 eV and −0.25 eV, respectively. All other parameters can be found in [2] except that we now find an optimum fit for a systematic error of +64 cm^{-1} affecting vibrational frequencies determined by DFT, $f(375\ K) = 1$ and the average slope a in Eq. (26) of [2] is equal to 1.8 10^{-3} K^{-1}. The resulting fit of the modified Redhead model predictions versus experimental TPR data remains very good (*rmsrd* 13%). We have also verified that according to this analytical model, the rate of production of H_2 by dissociative adsorption of H_2S on M-edge 50%S followed by associative desorption of H_2 (the reverse process of H_2 consumption/H_2S production) can be neglected (∼1.5% in average). This sequence of processes is nevertheless taken into account in the course of our kMC simulations.

It is worth noticing that combining Eqs. (20) and (14), and since $k^{KTG}_{g\to\phi}/K^{eq}_{g\to\phi} \gg k_{\phi\to\chi}$, the following approximation holds along the TPR1 peak:

$$k_{da} \approx \left(\frac{A_{st}}{A_{uc}}\right) k_{\phi\to\chi}\theta_\phi \tag{27}$$

Furthermore, and still under the steady-state approximation, the rate for associative desorption, the reverse process of dissociative adsorption, can be written as (indices H_2 or H_2S still implicit):

$$k_{ad} = \left(\frac{A_{st}}{A_{uc}}\right) \frac{k_{\chi\to\phi}k_{\phi\to g}}{k_{\chi\to\phi}\frac{\theta_\chi}{\theta_\phi} + k_{\phi\to g}}\theta_\chi \tag{28}$$

Since $k_{\chi\to\phi}\frac{\theta_\chi}{\theta_\phi} \ll k_{\phi\to g}$, the following approximation holds along the TPR1 peak:

$$k_{ad} \approx \left(\frac{A_{st}}{A_{uc}}\right) k_{\chi\to\phi}\theta_\chi \tag{29}$$

Therefore,

$$\frac{k_{ad}}{k_{da}} \approx \frac{k_{\chi\to\phi}\theta_\chi}{k_{\phi\to\chi}\theta_\phi} = \exp\left(\frac{-\Delta G^{\neq}_{\chi\to\phi} + \Delta G^{\neq}_{\phi\to\chi} - \Delta G_{g\to\chi} + \Delta G_{g\to\phi}}{k_B T}\right) = 1 \tag{30}$$

By Eq. (30), we have recovered the equality of the reverse and forward combined rates, as expected at equilibrium between the gaseous and chemisorbed states, and in coherence with the steady-state approximation leading to symmetric expressions for the forward and reverse equivalent rates, for two equilibrated steps in series.

These combined rates which emerge from a mean field analysis have dimensions of s^{-1}. As products of a spatial and a temporal probability, they define the probability that a dissociative chemisorption, or the reverse associative desorption event, happens at a given lattice site (e.g. one S_2 dimer in top site or two "half" adjacent H-bonded S–Mo–SH in top sites). These rates satisfy the micro-reversibility principle. It is therefore legitimate that we use them in our kMC simulations as pseudo microscopic rates, hence avoiding to consider separately as elementary events physisorption and dissociation, or association and desorption. These events have indeed rate constants that differ by so many orders of magnitude that in doing so one would waste essentially all simulation steps in physisorptions and desorptions. TPR simulations would remain stuck into negligible temperature/time intervals.

3. Results and discussion

3.1. Database of activation barriers

The barriers used for the 28 processes considered are listed in Table 1. As mentioned above, the results of direct DFT calculations are taken from Refs. [2,20] and [21]. Moreover, we have reconsidered the DFT data provided by Paul et al. [20] and, considering a variety of virtual channels, found that BEP relationships can describe this data, at least for dissociative adsorption of H_2 and associative desorption of H_2S on Mo-edges at S coverage ⩽50%, as illustrated in Fig. 7 and expressed below:

$$E^{\neq}_{ads\,H_2} = 1.079\Delta E_{ads\,H_2} + 0.454\ (\text{eV}) \tag{31}$$

$$E^{\neq}_{des\,H_2S} = 1.011\Delta E_{des\,H_2S} + 0.082\ (\text{eV}) \tag{32}$$

Notice that processes (21, 22) and (27, 28), which involve Mo-edges at S coverages >50% do not follow these particular BEP relationships.

Forward barriers $E^{\neq}$ corresponding to processes 11, 13 and 15 were estimated using first the BCS to evaluate the corresponding values of ΔE, then the BEP relationship found for dissociative adsorption of H_2. The reverse barriers for processes 12, 14 and 16 were deduced from the consistency requirement (CR) that the forward barrier equals the algebraic sum of reverse barrier and ΔE.

In order to assess the predictive value of our BCS approximation, we have performed comparative DFT calculations of energy differences associated with five processes involving the diffusion of H from top or bridge positions at M-edge. The results are reported in Table 2. We obtain a relatively poor correlation between the accurate and approximate energies ($E_{DFT} = 0.89E_{BCS}$, in eV, in the range −0.6 eV to 0.6 eV $R^2 = 0.63$). However, the BCS approximation does retain some predictive value: one should take care, however, to avoid using it in cases of processes with high barriers

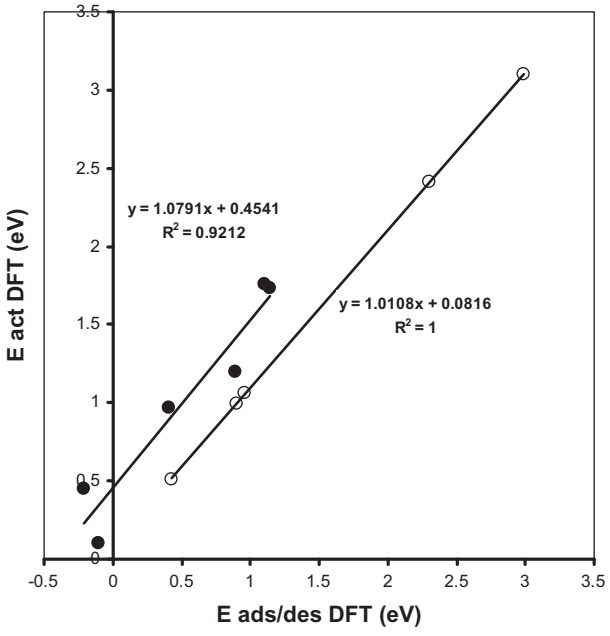

Fig. 7. Brönsted–Evans–Polanyi linear relationships between activation barriers (E act DFT) and adsorption or desorption energies (E ads/des DFT) resulting from the DFT calculations of Paul et al. [20] for the Mo-edge, starting from 50% S coverage. Open circles: (i) molecular or associative desorption of H_2S; filled circles: (ii) molecular or dissociative adsorption of H_2. All energies are given in eV. Insets indicate the parameters of linear regressions including squared coefficients of correlation R^2, being 1.000 and 0.921 for (i and ii) respectively. The regressed linear relationships are used for the estimated barrier values given in Table 1.

and potentially rate limiting, for which the best possible accuracy should be required.

Notice also that H_2 dissociative adsorption processes involved here are either homolytic (process 21, for 100%S M-edge) or heterolytic (processes 17 and 19 for 50%S M-edge and 33%S M-edge, respectively), as a results of exhaustive searches in the DFT investigations.

3.2. Experiments

Our simulations were tested against the same TPR experiments as described in our previous paper [2]. Namely, the TPR spectra of a consistent set of γ-Al_2O_3-supported MoS_2 catalysts with variable Mo content were compared to simulation. These results are summarized in Table 3 for the reader's convenience, while the experimental spectra are presented in Fig. SM1, which reproduces Fig. 3 of [2]. All catalysts were pre-sulfided in conditions chosen to produce a very high chemical potential of sulfur. These conditions are known to induce "triangular" morphologies of MoS_2 nanoparticles, containing only Mo-edges covered by S_2 dimers, that can be activated by reduction. The main observation was the occurrence in TPR of relatively narrow H_2 consumption peaks, for which the peak temperatures *decrease* with increasing Mo content. We have interpreted these low-temperature TPR peaks as corresponding to the reductive transition from S_2 dimer–covered Mo-edges to bridging S-covered Mo-edges, with S coverage decreasing from 100% to 50%. The peak integrals can be directly related to the edge content of the catalyst, or in other terms to the dispersion of the active element Mo. The peak temperature decreases with increasing Mo content because the dispersion loss is more than compensated for by the increased edge area when the MoS_2 particle density per unit area is close to constant.

The hypothesis of metastability of the initial "as prepared" morphology of gamma-alumina-supported MoS_2 nanoparticles along the recording of the first H_2 consumption/H_2S release peak in a TPR experiment may be challenged: these experiments involve flowing 25 cm^3 mn^{-1} of 5% vol H_2 in Ar at atmospheric pressure, temperature raised from 323 K up to 575 K at constant rate 0.1682 K s^{-1} until ca. 575 K within 25 mn. Notice that such a TPR experiment is essentially dynamic and in general, may sample states far from thermodynamic equilibrium. Moreover, we found that in the course of TPR experiments, according to the protocol followed, an almost constant release of H_2S by desorption from the gamma-alumina support alone occurred, measured at ca. 2 micromoles H_2S, for 56 micromoles H_2 per min introduced in the reactor [30]. The prevailing minimal H_2S/H_2 ratio during the experiment can thus be estimated at ca. 0.03 and it may reach twice this value at the TPR peak, when the rate of H_2S release by MoS_2 itself is maximal.

According to one of our previous works (see Fig. 1 in [31]), the relative chemical potential of sulfur imposed to the catalysts will then stay between −0.65 and −1 eV as the first peak is produced. Considering now the surface phase diagram established on the basis of our DFT calculations (see Fig. 3a in [5]), this trajectory is expected to correspond, at equilibrium, to a fraction of M-edges in the equilibrium morphology starting from 90% and ending at ca. 70%. Indeed, at equilibrium, at most 20% S-edge might appear, exclusively at 50% S coverage. To our knowledge, in the state of current experimental and simulation techniques, we cannot exclude that during TPR experiments, this equilibrium state is reached as it is also strongly suspected to be stabilized in real HDT conditions. Let us assume that a non-negligible amount of S-edge with 50% S coverage may exist. Paul and Payen [20] have found by DFT calculations that the limiting step to form a S-vacancy from a 50%S S-edge, the heterolytic association giving chemisorbed H_2S, has a total energy barrier of 1.69 eV. In that case, the modified Redhead model presented in our previous work [2] would predict a TPR peak temperature of 577 K for catalyst M-22, well above the experimental results (521 K), and in a zone where the TPR spectra exhibit minimal H_2 consumption.

We have therefore thermodynamic as well as kinetic arguments against a significant influence of S-edges in the TPR experiments. Besides, the observed persistence of gold-supported MoS_2 nanoparticles triangular morphologies prepared under H_2S exposure at high temperature (673 K), when observed by STM at ambient temperature and under secondary vacuum, as reported by Lauritsen et al. [32], is another experimental indication of the assumed tendency of such morphologies to get frozen in metastable states at least during the earlier stage of a TPR experiment.

Table 2
Comparison of energy differences obtained for some H diffusion processes on M-edge using the BCS approximation and accurate DFT calculations.

	BCS (eV)	DFT (eV)
$V_b + H_t + V_b + V_t \rightarrow V_b + V_t + H_b + V_t$	−0.56	−0.37
$S_b + H_t + S_b + V_t \rightarrow S_b + V_t + SH_b + V_t$	−0.14	+0.065
$SH_b + H_t + S_b + V_t \rightarrow SH_b + V_t + SH_b + V_t$	0.00	−0.22
$S_b + H_t + S_b + H_t \rightarrow S_b + V_t + SH_b + H_t$	0.30	0.00
$H_b + V_t + S_b + V_t \rightarrow V_b + V_t + SH_b + V_t$	0.42	0.53

3.3. kMC simulations

As mentioned above, the kinetic Monte Carlo simulations of the experimental TPR spectra were conducted with the improved H3 model for dissociative adsorption and associative desorption, as discussed above, on periodic 1D arrays of 1000 sites and repeated 10 times. The H3 model involves as inputs the energy barrier of 0.95 eV as reported in Table 1 for dissociative chemisorption, i.e. process 21, and parameter f representing the fraction of entropy retained in the molecular physisorbed state of hydrogen. For consistency, the value of f resulting from the new fit mentioned in Section 2.5 was used, namely $f(375\ K) = 1$, and the parameter a = 0.0018 K^{-1} representing the slope in the assumed linear variation of f with absolute temperature T.

Consistently with the experimental conditions discussed above, kMC simulations were run with imposed partial pressures of H_2 and H_2S, with $P_{H_2} = 5000$ Pa and $P_{H_2S} = 200$ Pa ($P_{H_2S}/P_{H_2} = 0.04$).

Table 3
Summary of TPR experiments results as reported in [2]: first peak temperatures TP1 and edge to basal area ratios α deduced from H_2 consumption during TPR experiments. The adimensional ratios (A_{st}/A_{uc}) of the area available for reactive adsorption to the total area available for adsorption, calculated according to Eq. (11) of [2], with data in columns Mo^{4+} and $\alpha = S/Mo^{4+}$, were used as inputs for the kMC simulations.

Ref.	Mo^{4+} (wt.%)	TP1 (K)	H_2 consumed below 600 K (μmol g^{-1})	$\alpha = S/Mo^{4+}$	(A_{st}/A_{uc})
Mo-4	3.53	552	128	0.348	0.0294
Mo-9	9.02	533.5	223	0.237	0.0580
Mo-12	11.07	530.4	248	0.215	0.0601
Mo-20	16.93	527.4	273	0.153	0.0721
Mo-22	20.92	521.2	289	0.133	0.0832

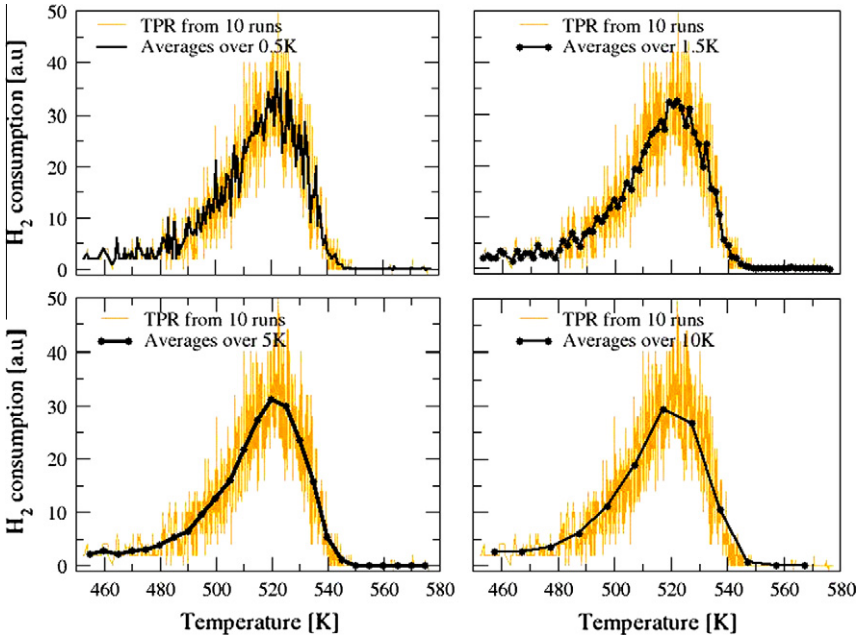

Fig. 8. Influence the width of temperature intervals used to average the raw data in kMC simulations of TPR. The case shown corresponds to catalyst Mo-22. The underlying highly noisy spectrum corresponds to the merged data points in the sub-interval [450–580 K] arising out of 10 independent simulations over the temperature interval [375–600 K]. The averaged data are shown as connected black dots. According to the notations and calculations presented in Section 2.2, the optimal number of temperature "bins" is L^* of order 200, so that the optimal averaging interval δT^* is close to 1 K (upper right): a high residual noise prevents the accurate location of the maximum and result in spurious peaks for too small a value of δT (upper left), while too much information is lost with intervals that are too large (lower left and right).

Each simulation represented ca. 100 h CPU of a 2.3 GHz node. As in the TPR experiments, the temperature was linearly increased from 450 K to 600 K with a heating rate of 0.1682 K s^{-1} (the actual rate measured in experiments, i.e. ca. 10 K mn^{-1}, as indicated in [2]). In order to account for the difference induced by the variable Mo loading in the catalysts under consideration, the prefactors (A_{st}/A_{uc}) for dissociative adsorption rates were used as inputs to the simulations. The values, listed in Table 3, were calculated using Eq. (11) of [2] and measurements of Mo^{4+} by XPS, while S in $\alpha = S/Mo^{4+}$ was given by the integral H_2S production in TPR (first peak) and specific areas by BET. All data are reported in [2].

Considerable attention was paid to the statistical post-processing of the kMC results. Due to the stochastic time step involved in kMC simulations and the shape of resulting TPR peaks, statistical averages have to be undertaken so as to maximize the information content according to our analysis in Section 2.2.

The influence of temperature intervals used to compute the averages over of a set of 10 kMC simulations is presented in Fig. 8, taking the example of catalyst Mo-22. An accurate location of the TPR peak temperature is essential. While sampling, intervals that are too narrow give rise to noisy results and show multiple spurious peaks, too broad an interval causes loss of information and again poor peak location. According to our estimates given in Section 2.2 for parameters corresponding to the conditions of our simulations, the optimal sampling interval should be of the order of 1 K as illustrated in the top right hand corner of Fig. 8.

Using this sampling approach, we compared the obtained kMC results with the kinetic interpretation, Fig. 9, and with the experimental TPR peaks, Fig. 10, both from [2]. Experimental and simulated TPR peaks were integrated using the Newton–Cotes method.

In Table 4, the fits are expressed as root mean square relative deviations (*rmsrd*), catalyst by catalyst and averaged, comparing

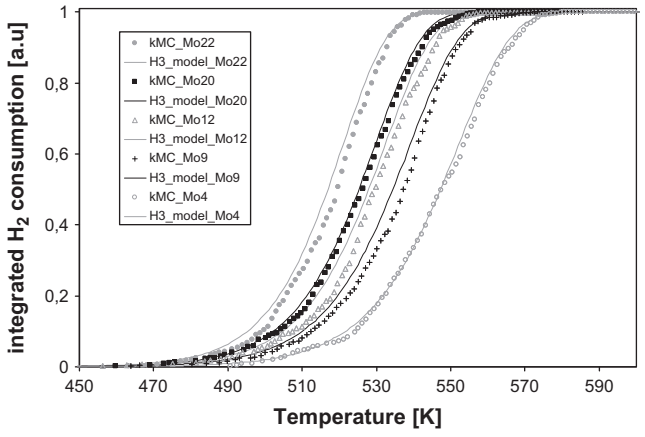

Fig. 9. Theoretical (full lines) and kMC (symbols) integrated TPR spectra for, from left to right, catalysts Mo-22, Mo-20, Mo-12, Mo-9 and Mo-4. The theoretical spectra correspond to the overall best fit using model H3.

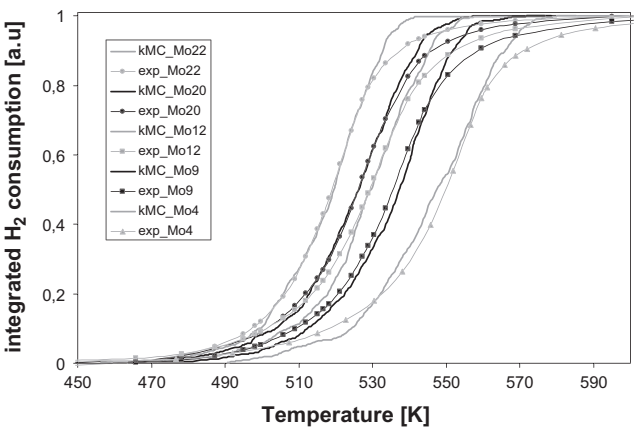

Fig. 10. Experimental (full lines with symbol) and kMC (thick lines) integrated TPR spectra for, from left to right, catalysts Mo-22, Mo-20, Mo-12, Mo-9 and Mo-4.

Table 4
Comparison of root mean square relative deviations (*rmsrd*) for integrated TPR spectra of catalysts Mo-22 to Mo-4. kMC results are compared with H3 analytical model (see [2]) predictions (*rmsrd* kMC/H3) and experimental data (*rmsrd* kMC/exp), H3 model predictions are compared with experimental data (*rmsrd* H3/exp).

Catalyst	*rmsrd* kMC/H3	*rmsrd* kMC/exp	*rmsrd* H3/exp
Mo-22	2.35	3.92	3.53
Mo-20	3.29	1.72	2.92
Mo-12	5.78	3.49	5.28
Mo-9	4.57	3.70	2.21
Mo-4	6.70	4.45	5.42
Average%	4.54	3.46	3.87

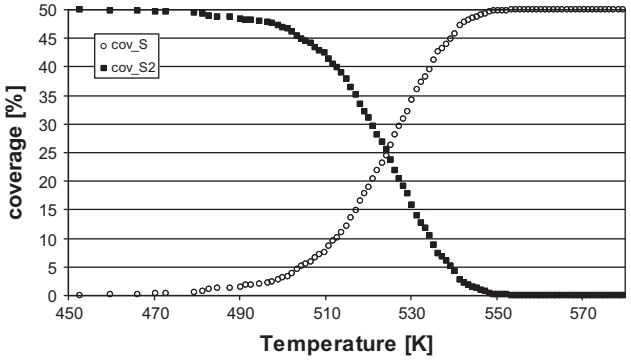

Fig. 11. Variation of coverages in sulfur dimers (filled squares) and bridging sulfur (open circles) for catalyst Mo-22 during a TPR simulation (% of bridge + top sites: initially S_2 occupy all top sites, see Fig. 2, while after completion of the reaction all bridge sites are occupied by bridging sulfur adatoms).

kMC to experiment, kMC to the analytical model of [2] and the analytical model to experiment. The averaged *rmsrd* are clearly similar in all cases, of the order of 4%, and represent a fairly good accuracy.

As shown in Fig. 11 with the example of Mo-22, these sets of kMC simulations allow us to illustrate the progressive depletion of S_2 dimers from the Mo-edges, giving way to bridging S adatoms S_b, and producing gaseous H_2S, as the TPR simulation progresses. It should be noticed that in this temperature interval corresponding to the first TPR peak, the dimers are exactly replaced by S_b so that void bridging sites (vacancies V_b) do not appear in the first peak. We cannot exclude that at higher temperature, such vacancies are formed but this remains beyond the scope of our study. Process 26 does occur, but is very disfavored by thermodynamics, and in presence of the background H_2S pressure imposed, it is much less frequent than the reverse process 25, which has a very low barrier. Process 24 has a very high barrier and is also extremely less probable than its reverse, process 23. Process 28 does not create a S-vacancy since as soon as the next top site becomes vacant, the S_t adatom is strongly stabilized in bridge position. Hence, for want of V_b sites, all H_2 dissociation channels ending in the formation of H_b at the expense of V_b cannot occur 13, 15, 19, and the same is true for their reverses 14, 16, 20. Surface diffusion 1 and 2, and surface associations 5 and 6 do not occur as well. Finally, two homolytic (11), (21) and one heterolytic H_2 dissociation (17) channels remain active, with comparable barriers. Process 11 has a relatively higher barrier and requires the extremely rare $V_t + V_b + V_t$ configuration of adjacent sites. Process 17 requires also the infrequent $S_b + V_t$ configuration of adjacent sites, while process 21 only requires a residual dimer on a top site: the latter appears therefore by far the most probable in our simulations. Finally, considering the associative desorption of H_2S from the dimers, it occurs mainly via process 28, the activation barrier of which is rather favorable (value of 0.73 eV) in comparison with that of process 22 involving H_2.

The good agreement obtained between the kMC simulations and both the experimental low-temperature TPR peaks and their analytical models increases confidence in the validity of the various assumptions underlying these simulations. However, we are conscious that more thorough inventories of all possible processes and more precise determinations of the associated barriers might result in a more complex picture.

Among the approximations made, the use of BCS to estimate energies and barriers is certainly the crudest, and DFT values should be preferred in the future. Moreover, the rather restricted set of available DFT energies and barriers should also be verified and extended. The BEP relationships reported here should be revisited accordingly and their basis understood in more detail. The contribution of lateral interactions between chemisorbed species should first be quantified through DFT calculations involving much larger unit cells (along the edge direction). Use of an effective Hamiltonian would limit the computational burden involved in the combinatorial explosion of configurations to be scrutinized in a kMC simulation as the range of interactions is increased.

We note however that since the rate-limiting step (*rls*) identified with the dissociative adsorption of dihydrogen sets the overall rate of reduction, the effect of the precise value of rates for all other elementary processes on the results will be small.

Besides, our first-principles-based kMC simulations do not depend on the metastability hypothesis already discussed in Section 3.2: we have explicitly simulated the TPR of initially 100%S-covered M-edges to give 50%S-covered M-edges, according to the reaction pathway determined at the DFT level and reported in [2]. The observed good correspondence between simulated and experimental H_2 consumptions curves should be taken as an *a posteriori* argument in favor of the metastability hypothesis (not a proof however). The same remark applies to our previous analytical interpretation based on a modified Redhead model as reported in [2]. Since the present report's primary purpose is to demonstrate the feasibility and the potential of kMC simulations to study the dynamics of elementary processes at active sites of model hydrotreating catalysts, we believe that bringing a demonstration of the metastability of the initial morphology is beyond our scope and propose to leave it as an interesting open question for future research.

4. Conclusions

In this report, we have presented the development and first results of a first-principles kinetic Monte Carlo simulation protocol aiming at the representation of elementary events at the active surfaces of industrial hydrotreating catalysts in operando. As a benchmark, we have chosen to attempt reproducing TPR experiments performed on unpromoted γ-Al_2O_3-supported MoS_2 nanoparticles previously reported and analyzed in depth [2]. Our conclusions are the following:

1. Linear arrays of alternating top and bridge sites constitute a valid representation of active edge surfaces for MoS_2-based hydrotreating catalysts.
2. kMC simulations match closely the experimental results of TPR spectra and their analytical interpretations, as long as one uses the same description as in the latter for the rates of dissociative adsorption and their reverse processes, associative desorption.
3. We have developed consistent expressions for these rates, which respect the micro-reversibility principle.
4. A limited DFT database may provide meaningful results, as long as the rate-limiting step is described to sufficient accuracy.
5. Large unit cells and repeated simulations are necessary in order to sample the phase space adequately and smooth inherently large fluctuations in local coverages.

6. A temperature interval which allows optimal statistical sampling can be determined for kMC simulations of TPR experiments.

Looking toward more applied considerations, this work proposes, as a development consistent with our previous study [2], a rational understanding of the low-temperature reduction peak observed in numerous TPR experiments on MoS_2-based catalysts. This result not only allows unambiguous identification of the so-called "weakly bonded S-species" released during the reduction process but also sheds new light on the elementary steps involved at the Mo-edge sites of the MoS_2 crystallites: i.e. the transformation of S_2 dimers into bridging sulfur monomers, as proposed in our previous work [2].

We are currently working on extensions and improvements of this kMC approach of the dynamical and equilibrium speciation at HDS catalysts active edge surface, including S-edges in unpromoted systems, and Co or Ni promoted M- and S-edges. We hope thus to be able to bring new insights into their activation by H_2 and the resulting effect of the promoter on the TPR diagram.

Acknowledgments

This work has been performed within the SIRE Project (Grant No. ANR-06-CIS6-014-04) sponsored by the Agence Nationale de la Recherche (ANR). The authors thank Pierre-Yves Prodhomme, who obtained the DFT calculations results presented in Table 2 during his recent postdoc at IFP.

Appendix A. Supplementary material

Supplementary data associated with this article can be found, in the online version, at doi:10.1016/j.jcat.2010.07.020.

References

[1] P. Afanasiev, Appl. Catal. A 303 (2006) 110.
[2] N. Dinter, M. Rusanen, P. Raybaud, S. Kasztelan, P. da Silva, H. Toulhoat, J. Catal. 267 (2009) 67.
[3] P. Raybaud, J. Hafner, G. Kresse, S. Kasztelan, H. Toulhoat, J. Catal. 189 (2000) 129.
[4] H. Schweiger, P. Raybaud, G. Kresse, H. Toulhoat, J. Catal. 207 (2002) 76.
[5] H. Schweiger, P. Raybaud, H. Toulhoat, J. Catal. 212 (2002) 33.
[6] J.V. Lauritsen, J. Kibsgaard, G.H. Olesen, P.G. Moses, B. Hinnemann, S. Helveg, J.K. Nørskov, B.S. Clausen, H. Topsøe, E. Laegsgaard, F. Besenbacher, J. Catal. 249 (2007) 220.
[7] J.V. Lauritsen, M. Nyberg, J.K. Nørskov, B.S. Clausen, H. Topsøe, E. Laegsgaard, F. Besenbacher, J. Catal. 224 (2004) 94.
[8] E.W. Hansen, M. Neurock, Chem. Eng. Sci. 54 (1999) 3411.
[9] J. Rogal, K. Reuter, M. Scheffler, Phys. Rev. Lett. 98 (2007) 046101.
[10] J. Rogal, K. Reuter, M. Scheffler, Phys. Rev. B 75 (2007) 205433.
[11] J. Rogal, K. Reuter, M. Scheffler, Phys. Rev. B 77 (2008) 155410.
[12] M. Neurock, D. Mei, Topics Catal. 20 (2002) 5.
[13] D. Mei, E.W. Hansen, M. Neurock, J. Phys. Chem. B 107 (2003) 798.
[14] A.B. Bortz, M.H. Kalos, J.L. Lebowitz, J. Comp. Phys. 17 (1975) 10.
[15] K.A. Fichthorn, W.H. Weinberg, J. Chem. Phys. 95 (1991) 1090.
[16] M. Matsumoto, T. Nishimura, ACM Trans. Model. Comput. Simul. 8 (1998) 3.
[17] W. Kohn, L.J. Sham, Phys. Rev. 140 (1965) A1133.
[18] G. Kresse, J. Furthmüller, Phys. Rev. B 54 (1996) 11169.
[19] G. Kresse, J. Furthmüller, Comput. Mater. Sci. 6 (1996) 15.
[20] J.F. Paul, E. Payen, J. Phys. Chem. B 107 (2003) 4057.
[21] A. Travert, H. Nakamura, R.A. van Santen, S. Cristol, J.F. Paul, E. Payen, J. Am. Chem. Soc. 124 (2002) 7084.
[22] J.N. Brønsted, K.J. Pedersen, Z. Phys. Chem. 108 (1924) 185.
[23] M.G. Evans, M. Polanyi, Trans. Faraday Soc. 32 (1936) 1333.
[24] M.G. Evans, M. Polanyi, Trans. Faraday Soc. 11 (1938) 34.
[25] T. Bligaard, J.K. Nørskov, S. Dahl, J. Matthiesen, C.H. Christensen, J. Sehested, J. Catal. 224 (2004) 206.
[26] J.K. Nørskov, T. Bligaard, J. Rossmeisl, H. Christensen, Nat. Chem. 1 (2009) 37.
[27] J.K. Nørskov, T. Bligaard, A. Logadottir, S. Bahn, L.B. Hansen, M. Bollinger, H. Bengaard, B. Hammer, Z. Sljivancanin, M. Mavrikakis, Y. Xu, S. Dahl, C.J.H. Jacobsen, J. Catal. 209 (2002) 275.
[28] H. Toulhoat, P. Raybaud, J. Catal. 216 (2003) 63.
[29] D. Loffreda, F. Delbecq, F. Vigné, P. Sautet, Angew. Chem. 121 (2009) 9140.
[30] P. da Silva, Ph.D. Thesis, University Paris 6, 1998.
[31] C. Arrouvel, M. Breysse, H. Toulhoat, P. Raybaud, J. Catal. 232 (2005) 161.
[32] J.V. Lauritsen, M.V. Bollinger, E. Lægsgaard, K.W. Jacobsen, J.K. Nørskov, B.S. Clausen, H. Topsøe, F. Besenbacher, J. Catal. 221 (2004) 510.